

Effects of ambient velocity shear on nonlinear internal wave associated mixing at the Columbia River plume front

Jiayi Pan^{1,2} and David A. Jay¹

Received 26 June 2008; revised 26 January 2009; accepted 18 March 2009; published 24 June 2009.

[1] Large-amplitude nonlinear internal waves (NLIWs) are frequently observed propagating away from Columbia River tidal plume fronts. They are generated because of the deceleration of the frontal bulge. During the River Influences on Shelf Ecosystems project cruises, the velocity, density structure and acoustic backscatter of the plume fronts and frontal NLIWs were observed using a towed vehicle, vessel-mounted instrumentation, and a vessel X band radar. These observations indicate that in the presence of strong ambient velocity shear, the NLIWs with maximum amplitudes occur well below the density interface and at a depth deeper than in the absence of shear. This deepening of the NLIW shear is associated with intensified vertical mixing below the interface. This is consistent with a dynamic analysis of NLIWs under the influence of sheared ambient flow, obtained from a high-order KdV model. There are two mechanisms responsible for the vertical turbulent mixing intensification. The nonlinear interaction between ambient shear and the NLIWs increases total velocity shear and causes the gradient Richardson number Ri_g to decrease below a critical value in certain depth ranges. Also, because of the presence of the ambient shear, the maximum NLIW velocity shear occurs at a depth below the density interface where there is less stratification.

Citation: Pan, J., and D. A. Jay (2009), Effects of ambient velocity shear on nonlinear internal wave associated mixing at the Columbia River plume front, *J. Geophys. Res.*, 114, C00B07, doi:10.1029/2008JC004988.

1. Introduction

[2] The tidal outflow from the Columbia River (CR) forms a coastal plume that is important to the coastal ecosystem [Barnes *et al.*, 1972; Grimes and Kingsford, 1996; Hickey *et al.*, 1998]. Observations indicated that the CR plume consists of four distinct water masses: (1) source water at the liftoff point and (2) the tidal, (3) the recirculating, and (4) the far-field plumes [Horner-Devine *et al.*, 2009]. The tidal plume is the water from the most recent ebb, with a radius of $\sim 10\text{--}30$ km. It is bounded by a distinct front that is the most energetic part of the plume and exhibits vigorous turbulent mixing, disturbing the seabed, dissipating plume energy and mixing upwelled nutrients and iron (Fe) from resuspended river sediments into the surface layer [Orton and Jay, 2005; E. D. Zaron and D. A. Jay, Mixing in the tidal plume of the Columbia River, submitted to *Journal of Geophysical Research*, 2008]. The salinity of the offshore plume is controlled by the ratio of horizontal advection to turbulent mixing [Nash *et al.*, 2009]. The initial expansion of the tidal plume is nearly radially symmetric and lowest-order properties can be reasonably predicted by a 1-D Lagrangian model (D. A. Jay *et al.*, Initial expansion of the Columbia

River tidal plume, submitted to *Journal of Geophysical Research*, 2008).

[3] The plume front often generates nonlinear internal waves (NLIWs) propagating offshore, and the generation occurs as the tidal plume front transitions from supercritical to subcritical conditions [Nash and Moum, 2005; Jay *et al.*, 2009]. These NLIWs are nonlinear solitary waves, or internal solitons. Pan *et al.* [2007] analyzed a group of internal solitons generated at and traveling offshore from the CR plume front using a satellite synthetic aperture radar (SAR) image and extracted the internal soliton dynamic parameters based on a theoretical model. Pan and Jay [2009] found that high-order KdV theory is preferable for description of dynamic properties of the CR plume frontal internal solitons. They demonstrated that the internal solitons transport mass seaward, expand the plume area by 3–20%, and can carry $\sim 75\%$ of the frontal energy out of the frontal region. Jay *et al.* [2009] reported that there are obvious differences in internal wave generation at upstream fronts between upwelling and downwelling conditions. Under typical downwelling conditions, the tidal plume front is usually broad (up to 5 km) and diffuse on its upstream southern side. However, under summer upwelling conditions, the upstream front remains sharp and narrow (only $\sim 20\text{--}50$ m wide on its upwind or northern side). NLIW generation is first seen on the southern side, and the front almost always “unzips” from south to north, regardless of upwelling status. However, NLIW generation is less common during periods of strong downwelling. Jay *et al.* suggested that potential vorticity conservation introduces an along-frontal asymmetry. It requires northerly fronts to

¹Department of Civil and Environmental Engineering, Portland State University, Portland, Oregon, USA.

²Also at Institute of Space and Earth Information Science, Chinese University of Hong Kong, Shatin, Hong Kong.

thin and accelerate, allowing them to remain supercritical for an extended period, up to 12 h.

[4] Frontal NLIWs have a major impact on the coastal ecosystem because the frontal internal waves can influence vertical mixing near the plume front and affect interaction of the tidal plume with plume near- and far-field waters. Many investigators documented mixing caused by internal waves. *Sandstrom et al.* [1989] argued that the shear intensified by internal waves could reduce the gradient Richardson number Ri_g . *Sandstrom and Oakey* [1995] found enhanced turbulent mixing on the Scotian Shelf occurring in a region with strong shear caused by internal waves. Observations of internal waves off the Oregon coast by *Moum et al.* [2003] showed high acoustic backscatter beginning in the vicinity of the internal wave trough and continuing through its trailing edge and wake. The acoustic backscatter coincided with overturning, high-density microstructure and turbulence at the interface. Nevertheless, the calculated Ri_g was larger than critical value of 0.25, suggesting a stable condition. They speculated that the acoustic Doppler current profiler (ADCP) time and space resolution did not allow capture of velocity shear caused by the internal waves. On the basis of high-resolution density measurements, they suggested the existence of a velocity layer with strong shear in the interface, which could produce the observed turbulence. Working in the same area, *Avicola et al.* [2007] reported that there were three factors contributing to the velocity shear and vertical mixing: the slowly varying thermal wind shear, the M2 internal tide, and near- f internal waves, all of which were of similar magnitude. When the three dominant shear constituents interfere constructively, enhanced turbulent mixing occurs.

[5] Clearly, it is common in coastal seas for NLIWs to coexist with ambient currents. This is particularly pertinent in the CR plume region, because NLIWs are frequently generated at the tidal plume front, an environment that often exhibits strong shear. *Stastna and Lamb* [2002] analyzed effects of a background shear on NLIWs using an analytical solution. They found that the background shear influences the amplitude and half-width of NLIWs relative to a zero-shear condition. The gradient Richardson number Ri_g was affected by the sheared background current as well, but no in situ observation was available to verify the analytical conclusions regarding wave properties. It remains uncertain, therefore, how the interaction of the ambient shear with NLIWs affects the mixing status. In this study, we analyze the CR frontal NLIWs under the influence of the ambient shear using data from the River Influenced Shelf ecosystems (RISE) project. Here, high-order KdV theory is used to explore dynamic mechanisms of the turbulent mixing induced by interaction between ambient shear and NLIWs. The study increases our knowledge of frontal mixing processes and their effects on the plume ecosystem.

2. RISE Observations

[6] RISE hypothesizes that waters influenced by the CR plume are more productive than adjacent coastal waters, especially off Washington. Understanding the impact of the highly mobile CR plume on coastal production and transport patterns requires that measurements be made on a variety of scales from turbulence to internal waves and fronts, to those

of the plume and the underlying shelf circulation. RISE emphasizes, therefore, rapid surveys and detailed process investigations.

[7] The RISE field program consists of 4 cruises in July 2004, June and August 2005, and June 2006. Each cruise was carried out by two vessels, the R/V *Wecoma* (biological and chemical studies) and the R/V *Pt Sur* (plume surveys, mixing processes and zooplankton dynamics). The R/V *Pt Sur* implemented rapid surveys using a towed body (TRIAXUS, steerable in 3-D) and the vessel's near-surface underway data acquisition system or UDAS. The high mobility of TRIAXUS was used to sample surface waters (from 60 m up to within 0.5–2 m of the surface, depending on sea state) outside of the ship wake. TRIAXUS carried an upward looking (REMUS configuration) 1200 kHz ADCP with mode 12 firmware, a 911 Seabird conductivity-temperature-depth (CTD) profiler [Pan and Jay, 2008]. The R/V *Pt Sur* UDAS acquired position, meteorological data, salinity (S), temperature (T), and fluorescence at 3 m. In addition, the R/V *Pt Sur* carried a pipe-mounted ADCP: 300 kHz in 2004 (RISE1) and 1200 kHz in 2005 and 2006 (RISE2 and RISE4). X band shipboard radar images were collected every minute during the 2006 RISE cruise. The ship radar images show sea surface roughness, and reveal the presence and properties of internal waves and plume fronts. This study uses the UDAS, X band radar and vessel ADCP data sets, along with CTD data from TRIAXUS.

[8] We seek here to contrast NLIW processes in situations with significant versus weak ambient shear as a means to understand the interaction of NLIW with ambient shear. The first situation pertained when we observed a NLIW packet on 10 June 2006 around 0230 UTC (6.85 h from high water). Figures 1a–1c show three shipboard radar images, taken on 10 June 2006 at 0229, 0249, and 0256 UTC, respectively. The NLIWs traveled from the CR plume front northwestward at 298°T . The cruise ship heading direction was 314°T . Therefore, the angle between the ship navigation and the NLIW traveling was 16° . The locations of the NLIW lines and fronts at these three times are illustrated in Figure 2 together with the bathymetry contours.

[9] Density profiles and ADCP data for the same time period are shown in Figure 3. Figure 3a is density profiles observed by the Seabird CTD onboard the TRIAXUS towfish. Figure 3a suggests that there are wave-like density undulations between longitude 124.292°W and 124.286°W . However, the TRIAXUS CTD cannot fully resolve NLIW structures, because the NLIW wavelength (~ 70 m) is considerably less than the cycle distance of the TRIAXUS (~ 300 m). Figures 3b and 3c show the horizontal crest-normal and vertical velocities, respectively. There are positive horizontal velocity anomalies relative to the background induced by the NLIWs (Figure 3b), suggesting that wave-induced water movements were in the direction of the wave traveling. On the leading edges of the NLIWs, the water particles move downward, and upward on the trailing edges, which causes a convergence zone on the leading edge and a divergence zone on the trailing one for each NLIW (Figure 3c). Figure 3d shows single-beam (beam 1) ADCP echo intensity, which better resolves the NLIW characteristics than the density data. Figure 3d also shows that there is intensified ADCP echo backscattering below the density

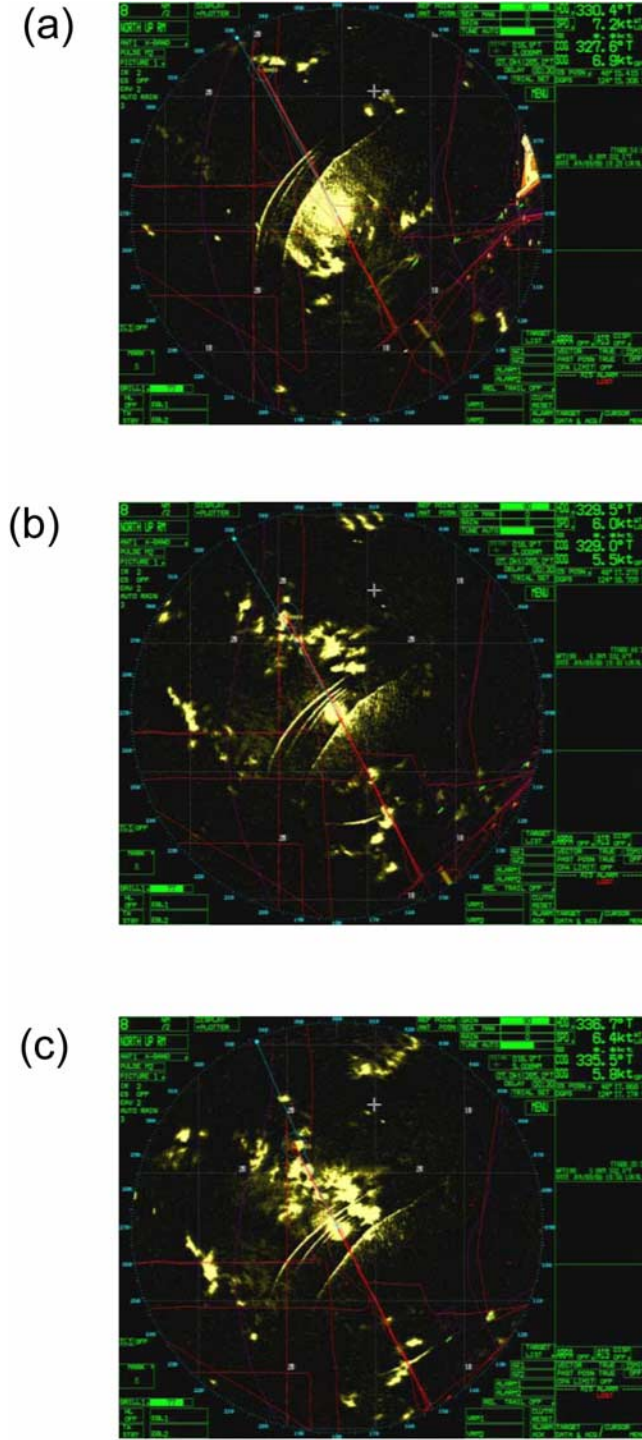


Figure 1. Shipboard X band radar images, taken on 10 June 2006 at (a) 0229, (b) 0249, and (c) 0256 UTC.

interface, suggesting that the NLIWs with maximum amplitudes are below the interface.

[10] The NLIWs in Figures 2 and 3 differ greatly from the NLIWs observed around 1400 UTC on 8 June 2006 and analyzed by *Pan and Jay* [2009]. Comparing the two cases, we notice a difference in ambient current conditions. In the first case (Figures 2 and 3), there is significant ambient current vertical shear, whereas for the second [*Pan and Jay*, 2009], the vertical shear is weak (Figure 4c). The presence

of ambient velocity shear is a likely reason for the different behavior of the NLIWs, a hypothesis we investigate here. *Pan and Jay* [2009] suggested that the high-order KdV model is better for modeling plume frontal NLIWs than weakly nonlinear NLIW theories. In the next section, on the basis of the high-order KdV model, we analyze the plume frontal NLIW dynamics under the influence of the ambient shear.

3. Dynamics of Frontal NLIWs Under Sheared Flow

[11] Two-dimensional internal waves may be described by a stream function ψ . The stream function is a product of linear wave speed $(c_0 - U)$ and the vertical displacement $A(x, z, t)$: $\psi = (c_0 - U) A(\chi, z)$, where $\chi = x - ct$; c_0 and c are the linear wave and NLIW speeds, respectively, and U is the ambient velocity. The vertical displacement has a separable form $A(x, z, t) = \eta(\chi)\phi(z)$, in which, $\phi(z)$ is the internal wave vertical structure function, satisfying the following eigenvalue equation

$$\frac{d}{dz} \left[(U - c_0)^2 \frac{d\phi}{dz} \right] + N^2 \phi = 0, \phi(0) = \phi(-H) = 0 \quad (1)$$

where c_0 is determined from eigenvalues, H is the water depth, and N is the buoyancy frequency for the undisturbed density ($N = \sqrt{-\frac{g}{\rho} \frac{\partial \rho}{\partial z}}$). The profile of density, buoyancy frequency, and ambient velocity for the first case are shown in

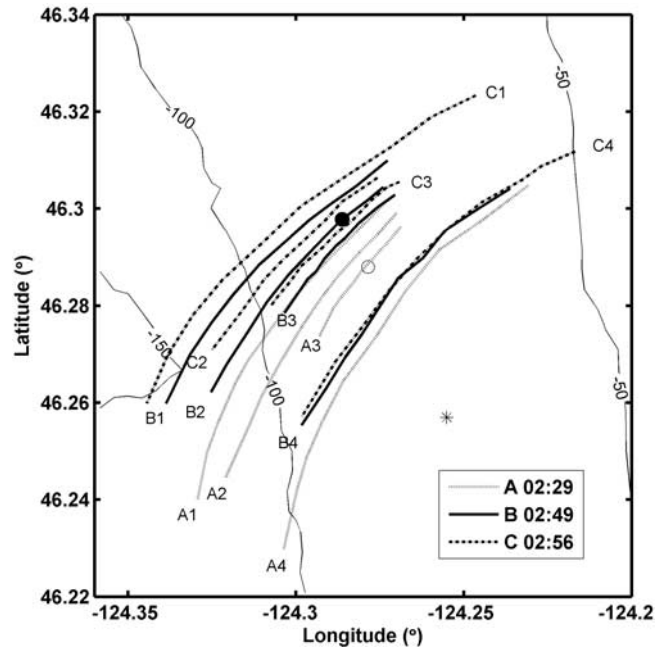


Figure 2. Georeferenced NLIW interpretations for 10 June 2006. The solid, thick solid, and dashed lines show the internal waves and fronts at 0229 (lines A1–A4), 0249 (lines B1–B4), and 0256 UTC (lines C1–C4), respectively. Lines A1–C1, A2–C2, and A3–C3 denote the leading, second, and third NLIWs, respectively, and lines A4–C4 show the plume fronts. The asterisk, hollow circle, and solid circle represent the ship locations at 0229, 0249, and 0256 UTC, respectively. The bathymetry contours are in meters.

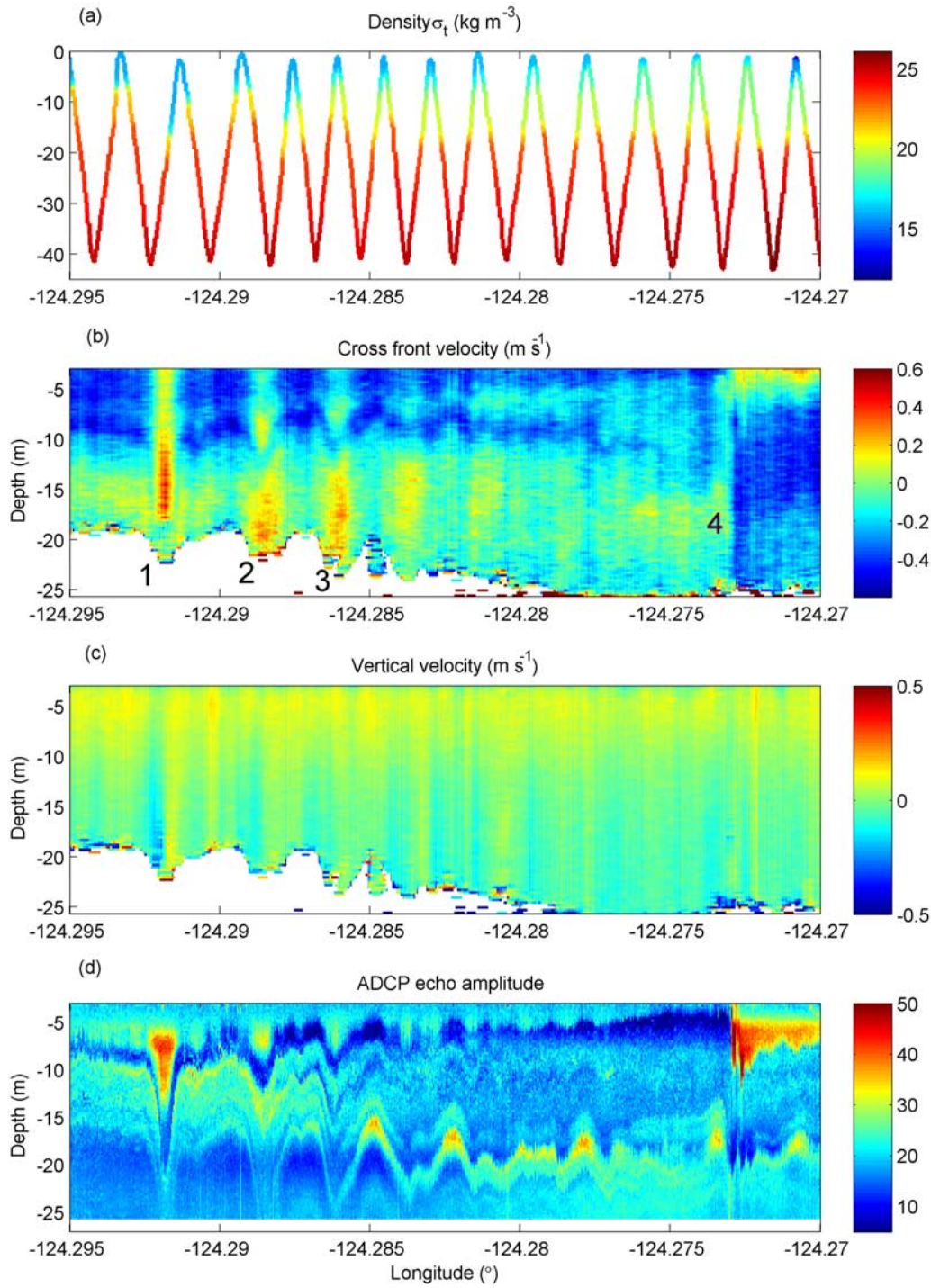


Figure 3. TRIAXUS CTD and ship mounted ADCP measurements on 10 June 2006 around 0230 UTC. (a) Density profiles by CTD, (b) ADCP crest-normal horizontal velocity, (c) vertical velocity, and (d) beam 1 ADCP echo intensity. The numbers 1, 2, 3, and 4 represent the internal waves and front shown in Figure 2.

Figure 4. The normalization condition is $\phi(z_{\max}) = 1$, where z_{\max} is the depth with the maximum value of ϕ . The NLIW amplitude η is governed by [Stanton and Ostrovsky, 1998; Ostrovsky and Stepanyants, 1989; Grimshaw et al., 2002]

$$\frac{\partial \eta}{\partial t} + (c_0 + \alpha \eta + \alpha_1 \eta^2) \frac{\partial \eta}{\partial x} + \beta \frac{\partial^2 \eta}{\partial x^2} = 0, \quad (2)$$

where

$$\alpha = \frac{3}{2} \frac{\int_{-H}^0 (c_0 - U)^2 (d\phi/dz)^3 dz}{\int_{-H}^0 (c_0 - U) (d\phi/dz)^2 dz}, \quad (3)$$

$$\beta = \frac{1}{2} \frac{\int_{-H}^0 (c_0 - U)^2 \phi^2 dz}{\int_{-H}^0 (c_0 - U) (d\phi/dz)^2 dz}. \quad (4)$$

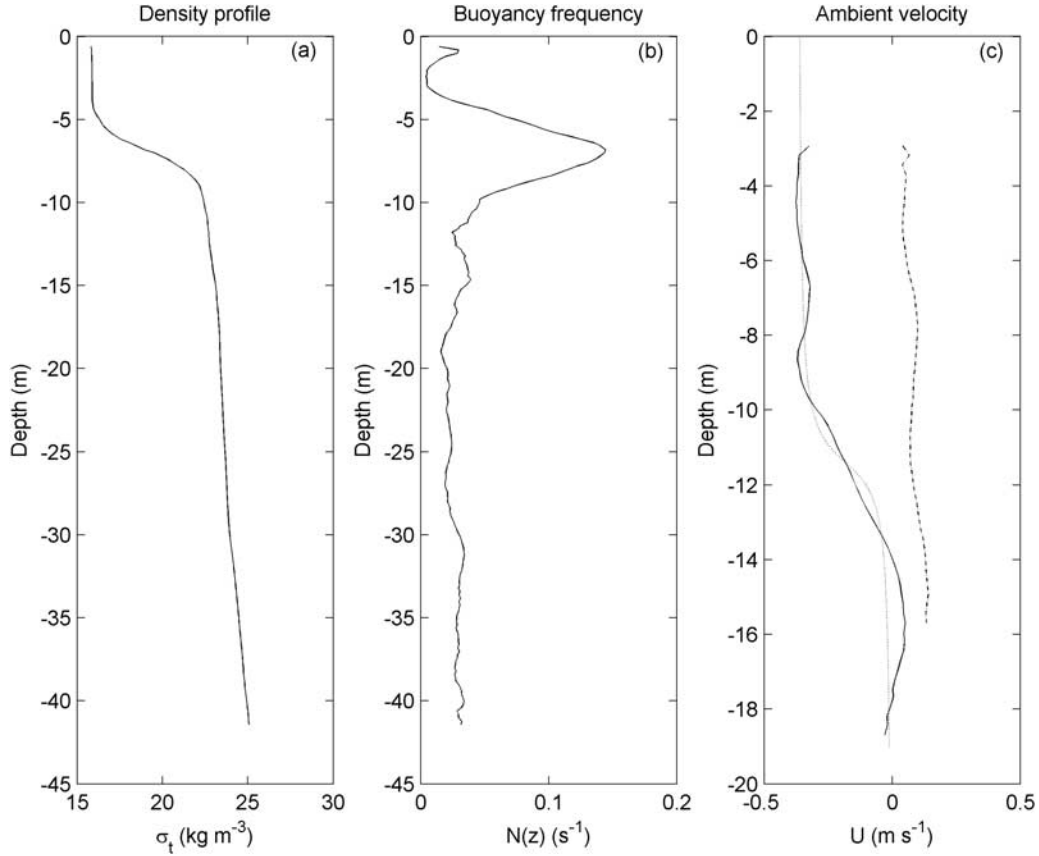


Figure 4. (a) The background density profile, (b) the observed buoyancy frequency, and (c) ambient velocity profiles for this study case (solid line) and for the NLIW case given by *Pan and Jay* [2009] (dash-dotted line). The three-parameter ambient velocity model is dashed.

The role of shear on coefficients α and β is evident from (3) and (4), but the coefficient α_1 in equation (2) is more complex [Holloway *et al.*, 2002],

$$\alpha_1 = \frac{1}{\int_{-H}^0 (c_0 - U)(d\phi/dz)^2 dz} \cdot \int_{-H}^0 \left\{ 3(c_0 - U)^2 \left[3d\xi/dz - 2(d\phi/dz)^2 \right] \cdot (d\phi/dz)^2 - \alpha^2 (d\phi/dz)^2 + \alpha(c_0 - U)(d\phi/dz) \cdot \left[5(d\phi/dz)^2 - 4d\xi/dz \right] \right\} dz, \quad (5)$$

where $\xi(z)$ is the first correction function to the NLIW mode; $\xi(z)$ is a solution to the following equation:

$$\frac{d}{dz} \left[(c_0 - U)^2 \frac{d\xi}{dz} \right] + N^2 \xi = -\alpha \frac{d}{dz} \left[(c_0 - U) \frac{d\phi}{dz} \right] + \frac{3}{2} \frac{d}{dz} \left[(c_0 - U)^2 \left(\frac{d\phi}{dz} \right)^2 \right], \quad (6)$$

with the boundary condition $\xi(0) = \xi(-H) = 0$ and normalized condition $\xi(z_{\max}) = 0$.

[12] For the high-order KdV equation (2), there is a soliton solution,

$$\eta = -\frac{\alpha}{\alpha_1} \frac{\nu}{2} \left[\tanh\left(\frac{x-ct}{\Delta} + \delta\right) - \tanh\left(\frac{x-ct}{\Delta} - \delta\right) \right], \quad (7)$$

where ν and δ are parameters satisfying

$$\delta(\nu) = \frac{1}{4} \ln\left(\frac{1+\nu}{1-\nu}\right), \quad (8)$$

and

$$\Delta = \sqrt{\frac{-24\alpha_1\beta}{\alpha^2\nu^2}}. \quad (9)$$

The NLIW phase speed is given by

$$c = c_0 - \frac{\alpha^2\nu^2}{6\alpha_1}. \quad (10)$$

[13] The internal wave vertical structure function (ϕ) and the first correction function (ξ) are obtained by solving (1) and (6) with the corresponding boundary conditions. We

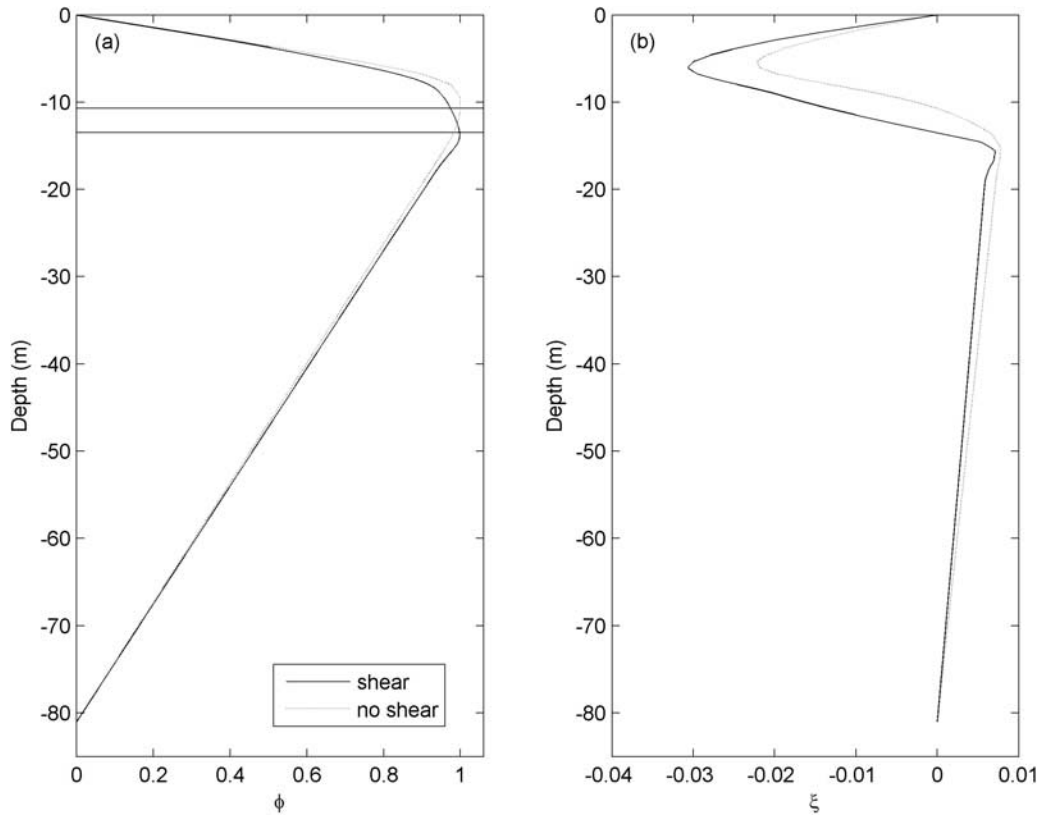


Figure 5. (a) The numerical solutions of the vertical structure function ϕ and (b) the first correction function ξ with ambient velocity shear (solid line) and without shear (dashed line).

employ the MATLAB partial differential equation (PDE) toolbox to obtain the numerical solutions to the differential equations. Only the first mode is considered because the phase speeds of higher-order modes are much slower than the first mode and even slower than the frontal speed, so that the higher-order modes cannot escape from the front.

[14] The solutions of ϕ and ξ to (1) and (6) are shown in Figures 5a and 5b with and without shear. The depth of maximum ϕ with ambient current shear is deeper in the water column than for the case without shear, suggesting that the ambient current shear modifies the vertical structures of the NLIWs. Without shear, z_{\max} is -10.7 m, whereas with shear, the z_{\max} is changed to -13.5 m. The vertical structure function ϕ and the correction function ξ are used to determine the parameters α , β , and α_1 by equations (3)–(5). These parameters are listed in Table 1. Larger differences are found between shear and no-shear conditions for α_1 than for α and β . The absolute value of α_1 and β , respectively, are five and two times smaller under the shear than no-shear condition, whereas α shows a 10% variation.

[15] The NLIW solutions to the high-order KdV equation can be compared to the observations. Using the ADCP echo intensity data (Figure 3d) and ship radar images (Figure 3), we extract the NLIW amplitude under and phase speed data, as per Pan and Jay [2009]. The predicted relationships between the NLIW phase speed and amplitude under shear and no-shear conditions are displayed in Figure 6, along with the observations in the case with shear (Table 2). The observations fit the model relationship closely. Compared with the no-shear condition, the NLIW amplitudes are larger

for the same phase speed and density stratification when shear is present.

[16] In order to determine the response of the solution to variations in the ambient shear, we use a three-parameter model to parameterize the ambient velocity and shear:

$$U_m(z) = U_0 \left\{ \frac{1}{\pi} \arctan \left[\frac{2(z + h_U)}{\delta h_U} \right] + \frac{1}{2} \right\}, \quad (11)$$

$$\frac{\partial U_m(z)}{\partial z} = U_{z0} \left[1 + \frac{4(z + h_U)^2}{\delta h_U^2} \right]^{-1}, \quad (12)$$

where U_m represents the modeled ambient velocity, h_U is the depth of the maximum ambient velocity shear, δh_U is the shear thickness, U_0 is approximately the surface layer ambient velocity, and $U_{z0} = 2U_0/(\pi\delta h_U)$ represents maximum velocity shear. The model parameters are listed in Table 3.

[17] The velocity profile and the model are shown in Figure 4c, together with the velocity profile with the weak shear in the case analyzed by Pan and Jay [2009]. We

Table 1. Environmental Parameters for the High-Order KdV Equations

	Parameters		
	α (s ⁻¹)	β (m ³ s ⁻¹)	α_1 (m ⁻¹ s ⁻¹)
Shear	-0.111	30.77	-0.0012
No shear	-0.108	68.07	-0.0064

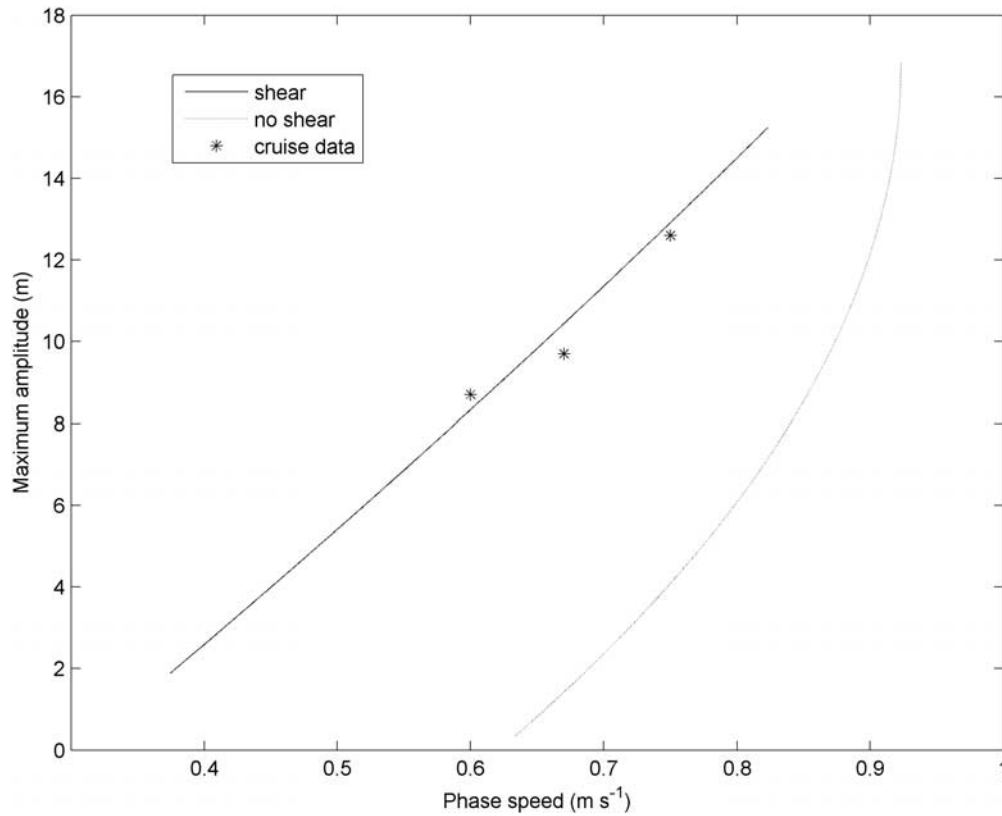


Figure 6. The theoretical relationships between the NLIW maximum amplitude and phase speed for ambient velocity shear (solid line) and no shear conditions (dashed line). The asterisks are the cruise measurement data points.

describe the sense of the ambient shear as “counter-NLIW” when surface ambient current is opposite the NLIW propagation; in this situation, U_0 , U_{z0} , and $\partial U_m(z)/\partial z$ are all <0 . The ambient shear is called “NLIW favorable” when both move in the same direction, so that U_0 , U_{z0} , and $\partial U_m(z)/\partial z$ are all >0 . As mentioned above, the ambient shear can influence the depth (z_{\max}) of NLIWs with maximum amplitudes. Figure 7 shows the dependence of z_{\max} on the ambient velocity shear parameters; U_{z0} exerts the strongest influence on z_{\max} . When ambient flow strengthens in counter-NLIW direction ($U_{z0} < 0$ and $|U_{z0}|$ increases), the depth of NLIWs with the largest amplitudes is deeper than that without shear. As ambient shear strengthens in NLIW favorable direction ($U_{z0} > 0$ and increases), the depth of the largest amplitude becomes shallower than the no-shear condition. Thus, counter-NLIW shear makes the NLIW deeper and the NLIW favorable ambient velocity shear forms a shallow NLIW structure. For the parameter range relevant at the present study, variations of h_U and δh_U do not affect z_{\max} (Figures 7b and 7c) until h_U is <5.5 m depth.

4. Interaction of NLIWs With Ambient Shear and Plume Mixing

[18] The occurrence of internal waves and their interaction with ambient shear may affect the vertical mixing of near-surface waters, especially in the presence of mean shear [Avicola *et al.*, 2007]. For NLIWs, this effect is more prominent because NLIWs may (1) greatly augment vertical

shear and (2) cause substantial isopycnal displacements, especially when the surface layer is thin, as is the case in the plume region. Above, it was demonstrated that the NLIW dynamic properties can be affected by the ambient shear. The NLIW exhibits maximum amplitude at a deeper depth. Thus, it is reasonable to consider the interaction between ambient shear and the NLIWs to be an important physical process that may affect upper ocean mixing, which is the subject of this section.

[19] In order to quantify the turbulent mixing status from observations, we calculate the turbulent kinetic energy (TKE) dissipation rate (ε) using the Thorpe scale method. Thorpe [1977] defined a turbulence length scale from density profiles. By sorting discrete density profiles into monotonic sequences, we can obtain displacements of water parcels

Table 2. Comparison of NLIW Properties From Vessel Data and Theory^a

	c (m s ⁻¹)	η_0 (m)
NLIW 1		
Cruise data	0.75	12.6
Model	0.75	12.9
NLIW 2		
Cruise data	0.67	9.7
Model	0.65	10.4
NLIW 3		
Cruise data	0.60	8.7
Model	0.61	8.3

^aFor all cases, soliton direction is 298° T, ship direction is 314° T, and ship speed is 2.7 m s⁻¹.

Table 3. Parameters for the Velocity Profile and Shear Models

	Model Parameters				
	U_0 (m s ⁻¹)	U_{z0} (s ⁻¹)	h_U (m)	σh_U (m)	H (m)
Values	-0.37	-0.16	-11.4	1.5	81.0

from the sorted density profiles. The Thorpe scale (L_T) is the RMS average of the displacements. Also, dissipation rate ε can be related to the Ozmidov scale L_O :

$$\varepsilon = L_O^2 N^3 \quad L_O = \varepsilon^{1/2} N^{-3/2}. \quad (13)$$

Several studies suggested that on average, L_O is related to L_T by [Crawford, 1986; Dillon and Park, 1987; Peters *et al.*, 1995; Peters, 1997]

$$L_O = C_L L_T, \quad (14)$$

where C_L is $O(1)$ [Peters and Johns, 2005; Orton and Jay, 2005]. Therefore, the TKE dissipation rate can be estimated as

$$\varepsilon = L_T^2 N^3. \quad (15)$$

[20] Figure 8 shows ADCP echo intensity and ε calculated from (15). It reveals two depth ranges in which ε is elevated; one at 5 to 10 m and the other at 13 to 20 m. However, the ambient shear (Figure 4c) is maximal between 9 to 13 m, and it does not match the depth ranges with high ε . Clearly, the elevated ε at 13–20 m is not directly caused by the ambient shear production, but it could be related to the deepening of

the NLIW shear production through the interaction between NLIW and ambient shear.

[21] To test this hypothesis, we derive the gradient Richardson number (Ri_g) with and without ambient shear. The ambient shear is taken from ADCP data, and the NLIW-induced shear is determined from the NLIW model. The NLIW horizontal velocity and its vertical shear can be obtained from the stream function

$$u = U + \frac{\partial \psi}{\partial z} = U + (c_0 - U) \eta \frac{\partial \phi}{\partial z} - \eta \phi \frac{\partial U}{\partial z}. \quad (16)$$

$$\frac{\partial u}{\partial \tilde{z}} = \frac{\partial U}{\partial \tilde{z}} + (c_0 - U) \eta \frac{\partial^2 \phi}{\partial \tilde{z} \partial \tilde{z}} - \eta \frac{\partial \phi}{\partial \tilde{z}} \frac{\partial U}{\partial \tilde{z}} - \eta \frac{\partial \phi}{\partial \tilde{z}} \frac{\partial U}{\partial \tilde{z}} - \eta \phi \frac{\partial^2 U}{\partial \tilde{z} \partial \tilde{z}}, \quad (17)$$

where \tilde{z} represents the NLIW disturbed vertical coordinate and $\tilde{z} = z + \eta \phi(z)$. Therefore, we have

$$d\tilde{z} = [1 + \eta \phi'(z)] dz, \quad (18)$$

where $\phi' = d\phi/dz$. Thus, the velocity shear is

$$\begin{aligned} \frac{\partial u}{\partial \tilde{z}} = & \frac{1}{1 + \eta \phi'} \frac{\partial U}{\partial z} + \frac{(c_0 - U) \eta}{1 + \eta \phi'} \frac{\partial^2 \phi}{\partial z^2} \\ & - \frac{2\eta}{1 + \eta \phi'} \frac{\partial \phi}{\partial z} \frac{\partial U}{\partial z} - \frac{\eta \phi}{1 + \eta \phi'} \frac{\partial^2 U}{\partial z^2}. \end{aligned} \quad (19)$$

The first term on the right-hand side is the ambient shear in isolation, the second is the NLIW shear in isolation, and the

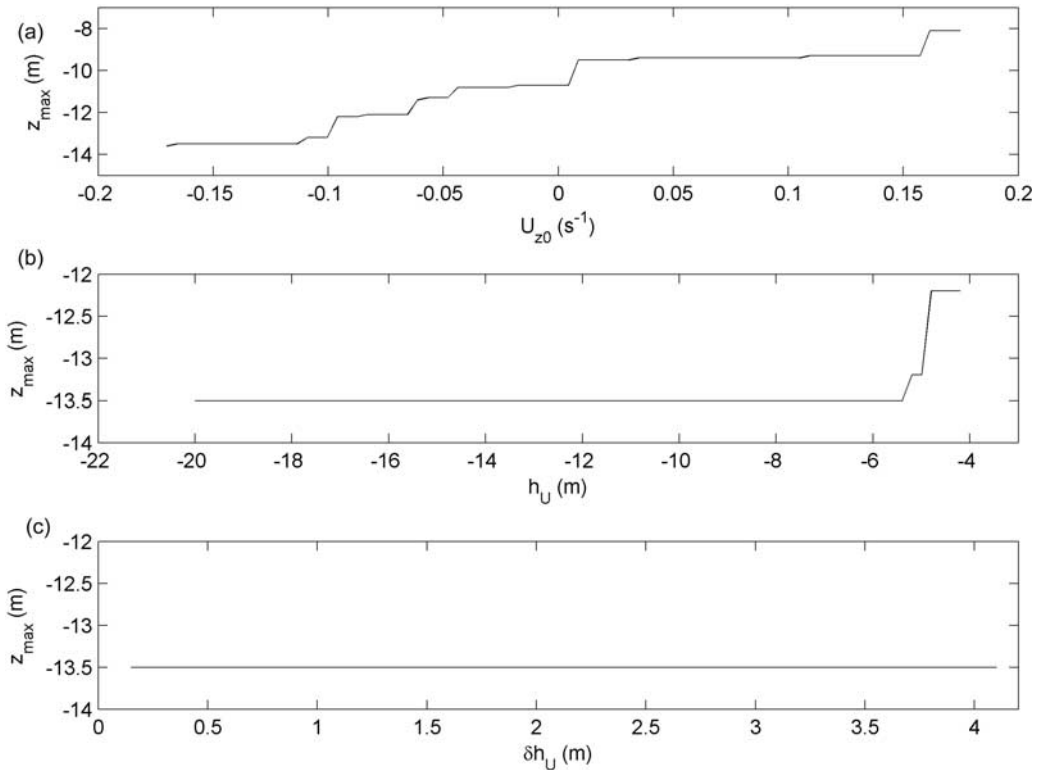


Figure 7. Relationships between the NLIW maximum amplitude depth and ambient velocity shear parameters (a) U_{z0} , (b) h_U , and (c) δh_U .

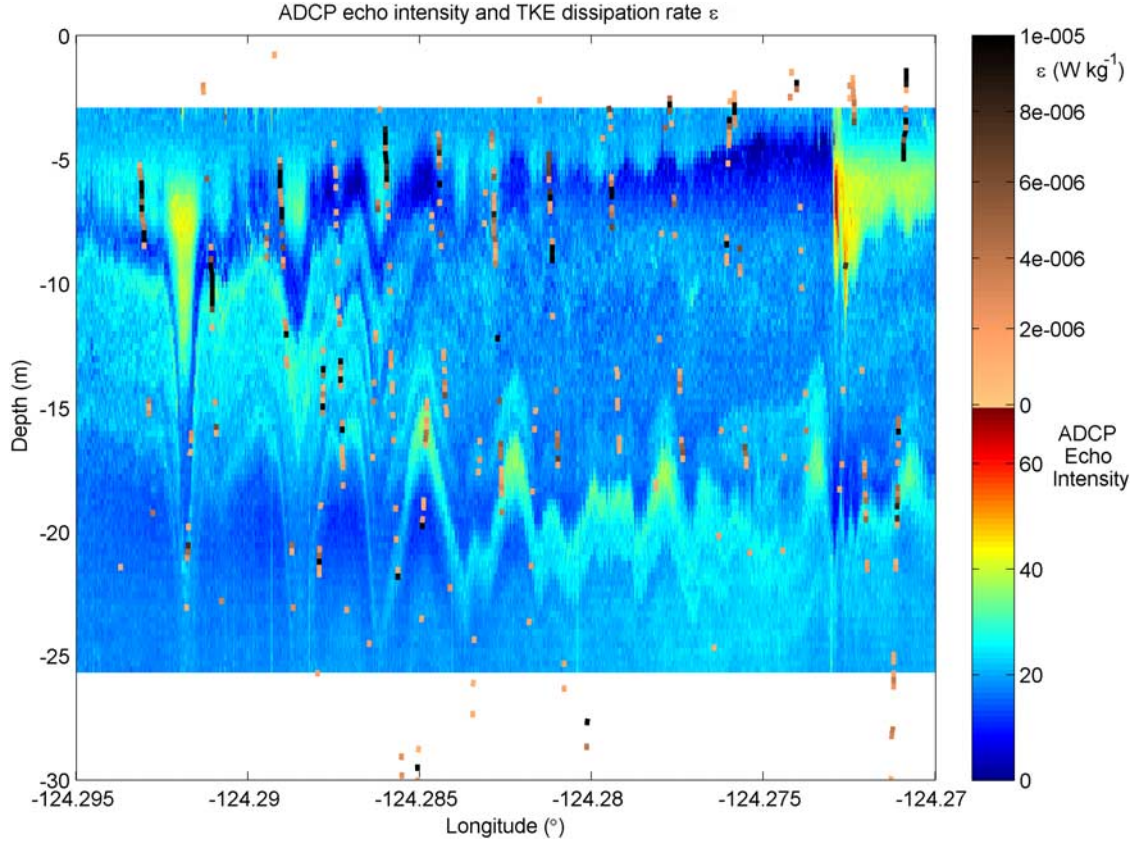


Figure 8. ADCP echo intensity and turbulent kinetic energy dissipation rate.

last two terms represent nonlinear interactions between the ambient shear and the NLIW shear. All four terms are, however, “warped” by the distortion of the vertical coordinate caused by the NLIW.

[22] The density vertical gradient is also modified by disturbance of the isopycnals, so the density gradient is

$$\frac{\partial \rho}{\partial \bar{z}} = \frac{1}{(1 + \eta \phi')} \frac{\partial \rho}{\partial z}. \quad (20)$$

The gradient Richardson number (Ri_g) is given by

$$Ri_g = \frac{-g \partial \rho / \partial \bar{z} / \rho}{(\partial u / \partial \bar{z})^2} = -\frac{1 + \eta \phi'}{\rho} \cdot \frac{g \partial \rho / \partial z}{[\partial U / \partial z + (c_0 - U) \eta \partial^2 \phi / \partial z^2 - 2 \eta (\partial \phi / \partial z) (\partial U / \partial z) - \eta \phi \partial^2 U / \partial z^2]^2}. \quad (21)$$

On the basis of (21), we calculate Ri_g at the center of the first NLIW, where the NLIW amplitude is $\eta = \eta_0$ (12.6 m), the profile of which is shown in Figure 9. There are two depth ranges below 7 m with Ri_g significantly less than the critical value of 0.25: (1) from 7.5 to 10 m and (2) between 13 and 19 m.

[23] The first depth range with $Ri_g < 0.25$ between 7.5–10 m also shows elevated ε (Figure 8). The shear in (19) is a superposition of the NLIW induced and ambient shears. Then the question is – what is the main factor responsible for a reduction of $Ri_g < 0.25$ between 7.5 and

10 m? In order to clarify this point, we analyze vertical profiles of NLIW dynamic properties. Figure 10 shows the profiles of $(c_0 - U)\eta_0$, ϕ , ψ [$= (c_0 - U)\eta_0 \phi$], u , $(du/dz)^2$, N^2 , and Ri_g . From 0 to 8 m, ϕ increases drastically (Figure 10b), whereas $(c_0 - U)\eta_0$ is relatively steady, but below 9 m, $(c_0 - U)\eta_0$ exhibits strong variations (Figure 10a). The product of the two terms $(c_0 - U)\eta_0$ and ϕ forms a peak between 7.5 and 10 m for ψ (Figure 10c). The water particle velocity consists of two components: one is the NLIW-induced velocity $u_{\text{NLIW}} (= d\psi/dz)$, and the other is the ambient velocity U . The total velocity is shown in the solid line in Figure 10d, and the ambient velocity U is in dash line. Figure 10d reveals that the scale of the total velocity is much greater than U , indicating that the NLIW-induced velocity shear is much stronger than ambient velocity shear. The total water particle velocity shear in (19) is close to the NLIW-induced velocity shear du_{NLIW}/dz , namely the second derivative of the stream function ψ ($d^2\psi/dz^2$). The maximum velocity shear appears at the depth of peak ψ , and so does the minimum Ri_g (Figures 10e and 10g). Thus, it appears that NLIW-induced shear is largely responsible for the reduction of Ri_g less than 0.25 between 7.5 and 10 m.

[24] The second depth range with total $Ri_g < 0.25$ in Figure 10 is between 13 and 19 m, consistent with the elevated ε in that depth range. By examining the profiles of $(c_0 - U)\eta_0$, ϕ , and ψ (Figures 10a–10c), we find that the peak velocity between 13 and 19 m is related to the interaction between the ambient velocity shear and the NLIW, that deepens the NLIWs. In this depth range, the ambient velocity shear modifies NLIW-induced velocity. Because both c_0

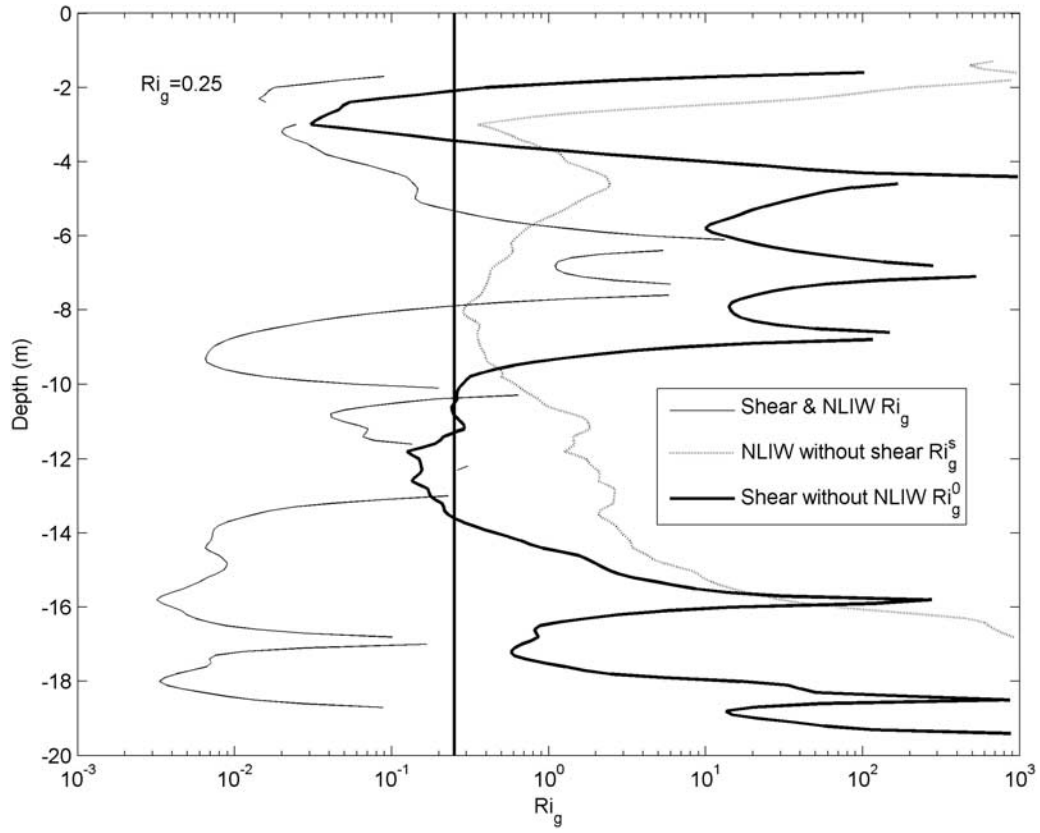


Figure 9. Total Ri_g resulting from the interaction of ambient velocity shear and NLIW (solid line), Ri_g^s for the NLIW but no ambient shear (dashed curve), and Ri_g^0 for ambient shear but no NLIW (thick curve).

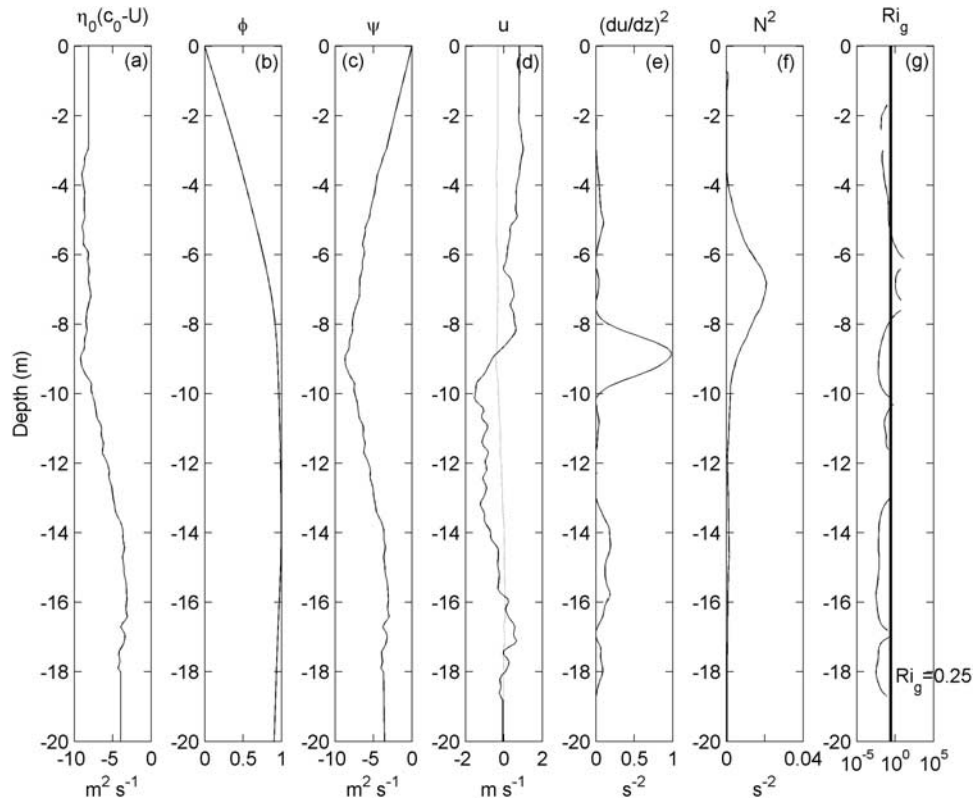


Figure 10. Profiles of (a) $(c_0 - U)\eta_0$, (b) ϕ , (c) ψ , (d) u , (e) $(du/dz)^2$, (f) N^2 , and (g) Ri_g .

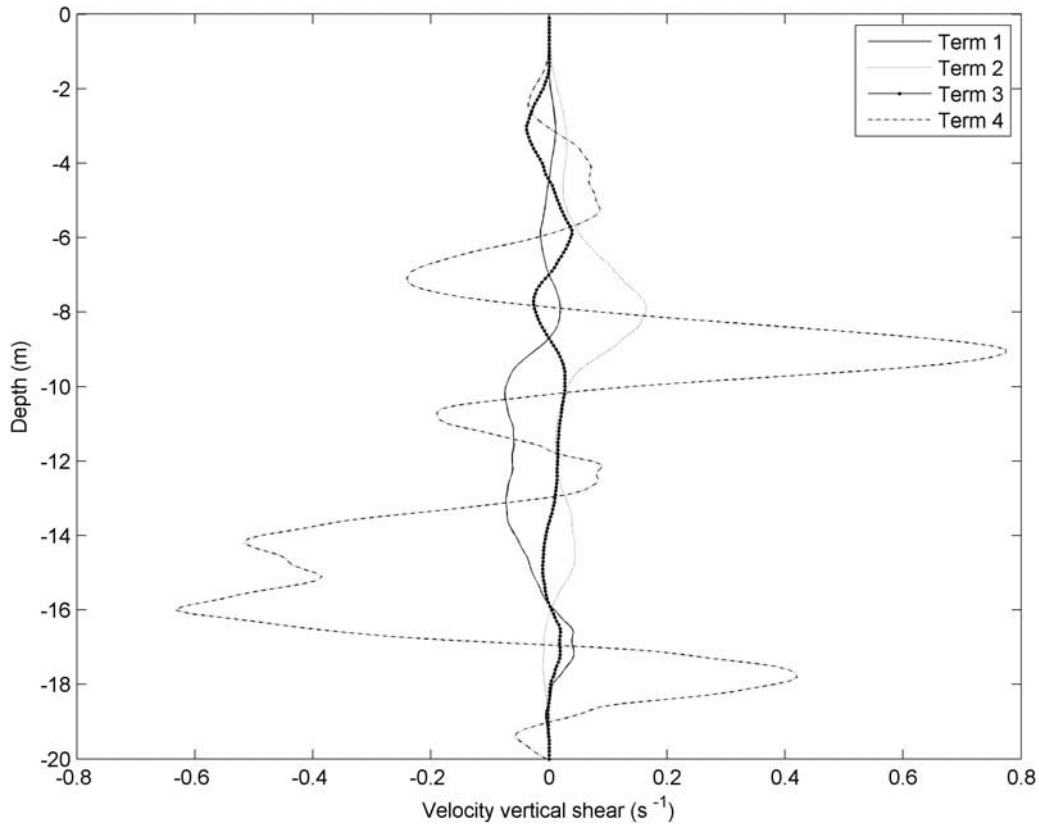


Figure 11. Profiles of the four terms on the right-hand side of equation (19). Term 1 is the ambient shear in isolation, term 2 is the NLIW shear in isolation, and terms 3 and 4 represent nonlinear interactions between the ambient shear and the NLIW shear.

and η_0 are constant, the profile of $(c_0 - U)\eta_0$ reflects the vertical variation of ambient velocity U . Figure 10a shows that the ambient velocity shear vanishes at the depth of NLIW maximum amplitude (13.5 m, Figure 10a), where there is an inflexion point in U (because $\partial U/\partial z = 0$). The combination of vertical structure function and the ambient velocity causes the NLIW stream function ψ to have an inflexion point at the depth as well (Figure 10c). We know that the total velocity shear is close to second derivative of ψ , and the total velocity shear reaches a local maximum at the inflexion point in ψ between 13 and 19 m (Figure 10e). Although the velocity shear in the depth between 13 and 19 m is smaller than that between 7.5 and 10 m (Figure 10e), Ri_g values in the two depth ranges are almost same. This is because N^2 is lower between 13 and 19 m than between 5 and 9 m (Figure 10f). Therefore, Ri_g at 13–19 m is reduced by the lower N^2 , whereas the effects of velocity shear between 7.5 and 10 m are partially compensated by the higher N^2 in this depth range.

[25] We can gain an overall appreciation of the factors leading to enhanced shear by comparing the magnitude of the four terms on the R.H.S of (19), as shown in Figure 11. The last two terms represent the nonlinear interaction between the ambient shear and NLIWs. Figure 11 shows that term 4 in (19) has much larger scale than other terms and dominates the velocity shear. The sign of the forth term is opposite between the upper and lower depths, revealing the opposite shear direction between the depths. This result suggests that the nonlinear interaction between ambient

shear and NLIWs is a primary factor leading to Ri_g reduction in areas where ambient shear and NLIW interact, at least given the parameters characteristic of the Columbia River plume area.

[26] We now examine the effects of ambient and NLIW shears on Ri_g . Ri_g in the absence of NLIWs is written as

$$Ri_g^0 = -\frac{g\partial\rho/\partial z}{\rho(\partial U/\partial z)^2}. \quad (22)$$

The result is shown in Figure 9 (Shear without NLIW). There is, however, a large difference between the total Ri_g (resulting from the combination of ambient shear and NLIW) and Ri_g^0 . Ri_g^0 is greater than Ri_g in the whole layer to 20 m depth, particularly in the two depth ranges with $Ri_g < 0.25$, 7.5 to 10 m and 13 to 19 m, where Ri_g^0 is almost > 0.25 . Below 4 m, only from 10 to 12 m appears $Ri_g^0 < 0.25$. Another depth range with Ri_g^0 below the critical value is between 2 and 3 m, possibly because of sample noise near the surface. Figure 9 also shows Ri_g for the NLIW without ambient shear (NLIW without shear), which is given by

$$Ri_g^s = -\frac{g\partial\rho/\partial z}{\rho c_0^* (d^2\phi^*/dz^2)^2}, \quad (23)$$

where c_0^* and ϕ^* are derived in the absence of ambient shear. Figure 9 reveals that Ri_g^s is > 0.25 at all depths. Thus, NLIWs alone cannot drive turbulent dissipation in this case.

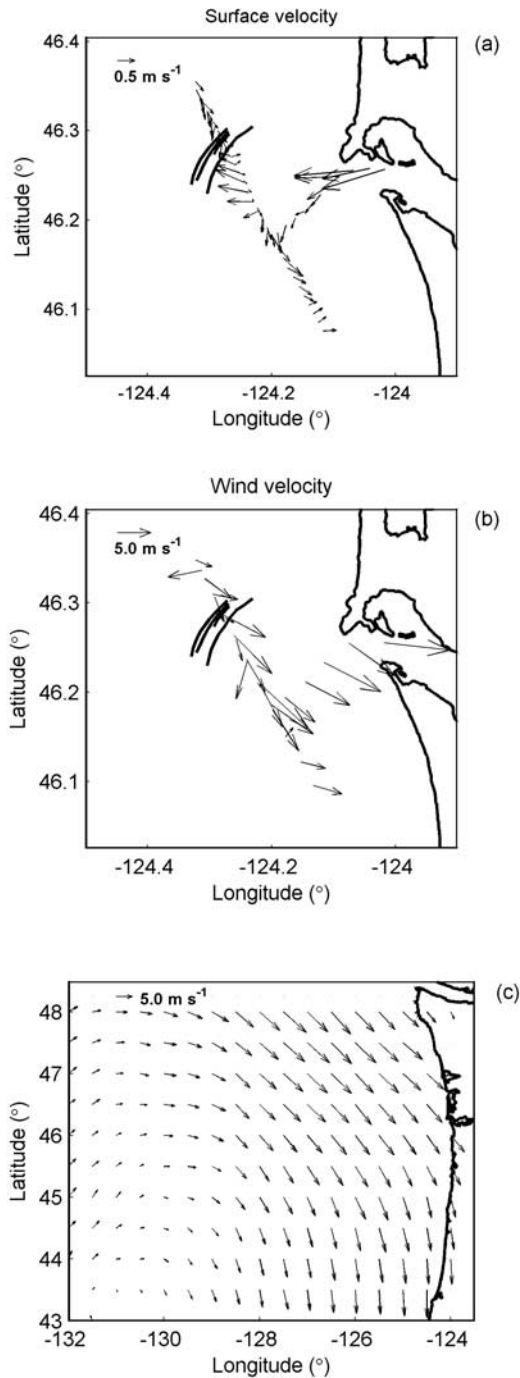


Figure 12. The cruise-measured (a) sea surface velocity and (b) wind velocity and (c) the large scale of satellite scatterometer winds over the northeast Pacific.

[27] In summary, the above analysis suggests that it is the nonlinear interaction between ambient shear and NLIWs, producing strong total velocity shear that sustains turbulent mixing. Ambient shear and NLIWs individually are inadequate to cause mixing, at least in the case analyzed here. The two mechanisms responsible for enhanced mixing are (1) enhanced shear due to the nonlinear interaction of ambient shear with the NLIW and (2) the displacement of

NLIW z_{\max} by ambient shear down from the interface to a level with lesser N^2 .

5. Discussion

[28] Results from the previous section show that the interaction between NLIW and ambient velocity shear can greatly modify the mixing status of the near surface waters in the tidal plume and near field. It is still necessary to identify mesoscale dynamic processes in the CR plume region that cause the ambient shear, and the connection between mesoscale dynamic processes and the mixing status of the CR plume region.

[29] Figure 12a shows ocean surface velocity measured by the ship-mounted ADCP along the ship cruise track for the period when ambient shear and NLIW interacted to drive mixing. The time period for the data shown in Figure 12a is from 0033 to 0613 UTC on 10 June 2006, 4.9~10.6 h after high water. The NLIWs appeared in this case, as they often do, during and after greater ebb. In the CR mouth, the surface current was strongly seaward, transporting surface plume water out of the CR estuary. Along the ship cruise track outside of the mouth and especially north of the NLIW train, we see that the surface current was flowing southward or southeastward (Figure 12a). The vessel wind velocity is shown in Figure 12b, in which northwesterly winds prevailed along the cruise track and suggest an upwelling condition. Figure 12c displays the large-scale vector wind field over the northeast Pacific on 10 June 2006 at 0000 UTC from QuikSCAT scatterometer observations. Northwesterly winds prevailed in the plume region, in accordance with the ship wind measurements. These upwelling favorable conditions occurred along the west flank of a large anticyclone over the northeast Pacific, and produced the coastal upwelling and the ambient velocity shear. Jay *et al.* [2009] observed that CR plume frontal internal waves occur more often under upwelling and neutral conditions than during downwelling, because these conditions favor the release of internal waves. Thus, particularly under upwelling and neutral conditions, the ambient velocity shear associated with the coastal upwelling regime can combine with NLIWs generated at the front to make the frontal region an actively mixing area.

[30] Strong ambient velocity shear may also be caused by internal tides in the CR plume region, giving rise to strong mean flow and NLIW interaction. This interaction could enhance NLIW-induced turbulent mixing as well, but we lack the data to quantify this effect.

6. Summary and Conclusions

[31] The tidal outflow of the Columbia River forms strong density stratification in the plume area waters off the river mouth, a condition which favors the occurrence of internal waves. The NLIWs are frequently observed to be generated at the tidal plume front and travel seaward from the front after high water. The presence of ambient velocity shears strongly influences the NLIW characteristics and consequent vertical mixing. When ambient shear is present, the NLIW with maximum amplitude is displaced downward as much as $O(5\text{ m})$ below the interface. We investigated the interaction of ambient shear and NLIWs via a numerical solution to

the NLIW vertical structure differential equation. The solution suggests that under the influence of the ambient velocity shear, the NLIW with maximum amplitude is displaced downward by the ambient velocity shear. The NLIW horizontal structure is investigated by the solution to the high-order KdV equation. The coefficients α , β , and α_1 of this KdV equation were determined using ambient density and velocity profiles obtained from vessel data. The actual phase speeds and amplitudes of the internal NLIW were measured using the shipboard X band radar images and in situ ADCP data, respectively. The velocity and amplitude relationship from the NLIW theory agreed well with observations.

[32] The presence of ambient velocity shear greatly affects NLIW induced turbulent mixing. We calculated the turbulent kinetic energy dissipation rate using the Thorpe scale method, which reveals two depth ranges with elevated turbulent dissipation in the form of numerous overturns. One is between 5 and 10 m, and the other is 13–20 m. Theoretical analysis suggests that where $Ri_g < 0.25$, the vertical velocity shear is intensified primarily by the interaction between sheared ambient velocity and the NLIW-induced velocity. At the deeper depth between 13 and 20 m, the decrease in N^2 leads to a reduction of Ri_g , so that although the velocity shear at 5–10 m is stronger than 13–20 m, Ri_g is almost the same in the two depth ranges. Neither ambient shear nor the NLIW could, in isolation, directly drive mixing for this case because $Ri_g > 0.25$ at all depths. Thus, the interaction of mean flow shear and NLIWs is an important factor creating conditions with $Ri_g < 0.25$, so that mixing may occur. The dominant mechanisms are (1) nonlinear interaction between ambient shear and NLIW and (2) downward displacement of the NLIW with maximum amplitude from the interface to a level where stability was lower.

[33] **Acknowledgments.** The study is supported by the National Science Foundation (project RISE–River Influences on Ecosystems, OCE 0239072) and partially by the direct grant of the Chinese University of Hong Kong. This is RISE contribution 32. We thank Captain Ron L. Short of the R/V *Pt Sur* and marine technicians Stewart Lamberdin and Ben Jokinen for their superb support of in situ data collection. The satellite scatterometer winds are obtained from the NASA/NOAA sponsored data system Seaflux at JPL through the courtesy of W. Timothy Liu and Wenqing Tang. The authors are grateful to the editors and anonymous reviewers for their valuable suggestions and comments.

References

- Avicola, G. S., J. N. Moum, A. Perlin, and M. D. Levine (2007), Enhanced turbulence due to the superposition of internal gravity waves and a coastal upwelling jet, *J. Geophys. Res.*, **112**, C06024, doi:10.1029/2006JC003831.
- Barnes, C. A., A. C. Duxbury, and B. A. Morse (1972), Circulation and selected properties of the Columbia River Effluent at sea, in *The Columbia River Estuary and Adjacent Ocean Waters*, edited by A. T. Pruter and D. L. Alverson, pp. 41–80, Univ. of Wash. Press, Seattle.
- Crawford, W. R. (1986), A comparison of length scales and decay times of turbulence in stratified flows, *J. Phys. Oceanogr.*, **16**, 1847–1854, doi:10.1175/1520-0485(1986)016<1847:ACOLSA>2.0.CO;2.
- Dillon, T. M., and M. M. Park (1987), The available potential energy of overturns as an indicator of mixing in the seasonal thermocline, *J. Geophys. Res.*, **92**, 5345–5353, doi:10.1029/JC092iC05p05345.
- Grimes, C. B., and M. J. Kingsford (1996), How do riverine plumes of different sizes influence fish larvae: Do they enhance recruitment?, *Mar. Freshwater Res.*, **47**, 191–208, doi:10.1071/MF9960.191.
- Grimshaw, R., D. Pelinovsky, E. Pelinovsky, and A. Slunyaev (2002), Generation of large-amplitude solitons in the extended Korteweg-de Vries equation, *Chaos*, **12**, 1070–1076, doi:10.1063/1.1521391.
- Hickey, B. M., L. J. Pietrafesa, D. A. Jay, and W. C. Boicourt (1998), The Columbia River plume study: Subtidal variability in the velocity and salinity fields, *J. Geophys. Res.*, **103**, 10339–10368, doi:10.1029/97JC03290.
- Holloway, P., E. Pelinovsky, and T. Talipova (2002), Internal tide transformation and oceanic internal solitary waves, in *Environmental Stratification Flows*, edited by R. Grimshaw, pp. 29–60, Kluwer Acad., Boston, Mass.
- Horner-Devine, A., D. A. Jay, P. M. Orton, and E. Spahn (2009), A conceptual model of the strongly tidal Columbia River plume, *J. Mar. Syst.*, in press.
- Jay, D. A., J. Pan, P. M. Orton, and A. Horner-Devine (2009), Asymmetry of tidal plume fronts in an Eastern Boundary Current regime, *J. Mar. Syst.*, in press.
- Moum, J. N., D. M. Farmer, W. D. Smyth, L. Armi, and S. Vagle (2003), Structure and generation of turbulence at interfaces strained by internal solitary waves propagating shoreward over the continental shelf, *J. Phys. Oceanogr.*, **33**, 2093–2112, doi:10.1175/1520-0485(2003)033<2093:SAGOTA>2.0.CO;2.
- Nash, J. D., and J. N. Moum (2005), River plumes as a source of large-amplitude internal waves in the coastal ocean, *Nature*, **437**, 400–403, doi:10.1038/nature03936.
- Nash, J. D., L. Kilcher, and J. N. Moum (2009), The structure and composition of a strongly-stratified, tidally-pulsed river plume, *J. Geophys. Res.*, doi:10.1029/2008JC005036, in press.
- Orton, P. M., and D. A. Jay (2005), Observations at the tidal plume front of a high-volume river outflow, *Geophys. Res. Lett.*, **32**, L11605, doi:10.1029/2005GL022372.
- Ostrovsky, L. A., and Y. A. Stepanyants (1989), Do internal solitons exist in the Ocean?, *Rev. Geophys.*, **27**, 293–310, doi:10.1029/RG027i003p00293.
- Pan, J., and D. A. Jay (2008), A method for Triaxus ADCP velocity data processing, *J. Atmos. Oceanic Technol.*, **25**, 1710–1716, doi:10.1175/2008JTECH0534.1.
- Pan, J., and D. A. Jay (2009), Dynamic characteristics and horizontal transports of internal solitons generated at the Columbia River plume front, *Cont. Shelf Res.*, **29**, 252–262, doi:10.1016/j.csr.2008.01.002.
- Pan, J., D. A. Jay, and P. M. Orton (2007), Analyses of internal solitary waves generated at the Columbia River plume front using SAR imagery, *J. Geophys. Res.*, **112**, C07014, doi:10.1029/2006JC003688.
- Peters, H. (1997), Observations of stratified turbulent mixing in an estuary. Neap-to-spring variations during high river flow, *Estuarine Coastal Shelf Sci.*, **45**, 69–88, doi:10.1006/ecss.1996.0180.
- Peters, H., and W. E. Johns (2005), Mixing and entrainment in the Red Sea outflow plume, part II: Turbulence characteristics, *J. Phys. Oceanogr.*, **35**, 584–600, doi:10.1175/JPO2689.1.
- Peters, H. M., C. Gregg, and T. B. Sanford (1995), Detail and scaling of turbulent overturns in the Pacific Equatorial Undercurrent, *J. Geophys. Res.*, **100**, 18,349–18,368.
- Sandstrom, H., and N. S. Oakey (1995), Dissipation in internal tides and solitary waves, *J. Phys. Oceanogr.*, **25**, 604–614, doi:10.1175/1520-0485(1995)025<0604:DIITAS>2.0.CO;2.
- Sandstrom, H., J. A. Elliott, and N. A. Cochrane (1989), Observing groups of solitary internal waves and turbulence with BATFISH and Echo-sounder, *J. Phys. Oceanogr.*, **19**, 987–997, doi:10.1175/1520-0485(1989)019<0987:OGOSIW>2.0.CO;2.
- Stanton, T. P., and L. A. Ostrovsky (1998), Observations of highly nonlinear internal solitons over the continental shelf, *Geophys. Res. Lett.*, **25**, 2695–2698, doi:10.1029/98GL01772.
- Stastna, M., and K. G. Lamb (2002), Large fully nonlinear internal solitary waves: The effect of background current, *Phys. Fluids*, **14**, 2987–2999, doi:10.1063/1.1496510.
- Thorpe, S. A. (1977), Turbulence and mixing in a Scottish loch, *Philos. Trans. R. Soc. London, Ser. A*, **286**, 125–181, doi:10.1098/rsta.1977.0112.

D. A. Jay and J. Pan, Department of Civil and Environmental Engineering, Portland State University, Portland, OR 97201, USA. (panj@cecs.pdx.edu)